The Power Spectral Properties of the Z Source GX 340+0

Jonker, Peter G.; van der Klis, Michiel; Wijnands, Rudy; Homan, Jeroen; van Paradijs, Jan; Méndez, Mariano; Ford, Eric C.; Kuulkers, Erik; Lamb, Frederick K.

Published in:
The Astrophysical Journal

DOI:
10.1086/309029

THE ASTROPHYSICAL JOURNAL, 537:374–386, 2000 July 1

THE POWER SPECTRAL PROPERTIES OF THE Z SOURCE GX 340+0

PETER G. JONKER,[1] MICHIEL VAN DER KLIS,[1] RUDY WIJNANDS,[1,2] JEROEN HOMAN,[1] JAN VAN PARADIJS,[1,3] MARIANO MÉNDEZ,[1,4] ERIC C. FORD,[1] ERIK KUULKERS,[5,6] AND FREDERICK K. LAMB[7]

Received 1999 November 30; accepted 2000 February 7

ABSTRACT

We present an analysis of ~390 ks of data of the Z source GX 340+0 taken during 24 observations with the *Rossi X-Ray Timing Explorer* satellite. We report the discovery of a new broad component in the power spectra. The frequency of this component varied between 9 and 14 Hz and remained close to half that of the horizontal-branch quasi-periodic oscillations (HBOs). Its rms amplitude was consistent with being constant around ~5%, while its FWHM increased with frequency from 7 to 18 Hz. If this sub-HBO component is the fundamental frequency, then the HBO and its second harmonic are the second and fourth harmonic component, while the third harmonic was not detected. This is similar to what was recently found for the black hole candidate XTE J1550−564. The profiles of both the horizontal- and the normal-branch quasi-periodic oscillation peaks were asymmetric when they were strongest. We describe this in terms of a shoulder component at the high-frequency side of the quasi-periodic oscillation peak, of which the rms amplitudes were approximately constant at ~4% and ~3%, respectively. The peak separation between the twin kilohertz quasi-periodic oscillations was consistent with being constant at 339±8 Hz, but a trend similar to that seen in, e.g., Sco X-1 could not be excluded. We discuss our results within the framework of the various models that have been proposed for the kilohertz QPOs and low-frequency peaks.

Subject headings: accretion, accretion disks — stars: individual (GX 340+0) — stars: neutron — X-rays: stars

1. INTRODUCTION

GX 340+0 is a bright low-mass X-ray binary (LMXB) and a Z source (Hasinger & van der Klis 1989). The Z-shaped track traced out by Z sources in the X-ray color-color diagram or hardness-intensity diagram (HID) is divided into three branches: the horizontal branch (HB), the normal branch (NB), and the flaring branch (FB). The power spectral properties and the HID of GX 340+0 were previously described by van Paradijs et al. (1988) and Kuulkers & van der Klis (1996) using data obtained with the *EXOSAT* satellite, by Penninx et al. (1991) using data obtained with the *Ginga* satellite, and by Jonker et al. (1998) using data obtained with the *Rossi X-Ray Timing Explorer* (*RXTE*) satellite. An extra branch trailing the FB in the HID has been described by Penninx et al. (1991) and Jonker et al. (1998). When the source is on the HB or on the upper part of the NB, quasi-periodic oscillations (QPOs) occur with frequencies varying from 20 to 50 Hz: the horizontal-branch quasi-periodic oscillations or HBOs (Penninx et al. 1991; Kuulkers & van der Klis 1996; Jonker et al. 1998). Second harmonics of these HBOs were detected by Kuulkers & van der Klis (1996) and Jonker et al. (1998) in the frequency range 73–76 Hz and 38–69 Hz, respectively. In the middle of the NB, van Paradijs et al. (1988) found normal-branch oscillations (NBOs) with a frequency of 5.6 Hz. Recently, Jonker et al. (1998) discovered twin kilohertz QPOs in GX 340+0. These QPOs have now been seen in all six originally identified Z sources (Sco X-1, van der Klis et al. 1996; Cyg X-2, Wijnands et al. 1998b; GX 17+2, Wijnands et al. 1997b; GX 349+2, Zhang, Strohmayer, & Swank 1998; GX 340+0, Jonker et al. 1998; GX 5-1, Wijnands et al. 1998a; see van der Klis 1998, 1999 for reviews), but not in Cir X-1, which combines Z source and atoll source characteristics (Oosterbroek et al. 1995; Shirey, Bradt, & Levine 1999; see also Psaltis, Belloni, & van der Klis 1999b).

In the other class of LMXBs, the atoll sources (Hasinger & van der Klis 1989), kilohertz QPOs are observed as well (see van der Klis 1998, 1999 for reviews). Recently, also HBO-like features have been identified in a number of atoll sources (4U 1728−34, Strohmayer et al. 1996, Ford & van der Klis 1998, Di Salvo et al. 2000; GX 13+1, Homan et al. 1998; 4U 1735−44, Wijnands et al. 1998c; 4U 1705−44, Ford, van der Klis, & Kaaret 1998a; 4U 1915−05, Boirin et al. 1999; 4U 0614+09, van Straaten et al. 1999; see Psaltis et al. 1999b for a summary). Furthermore, at the highest inferred mass accretion rates, QPOs with frequencies near 6 Hz have been discovered in the atoll sources 4U 1820−30 (Wijnands, van der Klis, & Rijkhorst 1999b), and XTE J1806−246 (Wijnands & van der Klis 1998b, 1999a; Revnivtsev, Borozdin, & Emelyanov 1999), which might have a similar origin as the Z source NBOs.

At low mass accretion rates, the power spectra of black hole candidates, atoll, and Z sources show similar characteristics (van der Klis 1994a, 1994b). Wijnands & van der Klis (1999b) found that the break frequency of the broken power law that describes the broadband power spectrum correlates well with the frequency of peaked noise components (and sometimes narrow QPO peaks) observed in

[1] Astronomical Institute "Anton Pannekoek," University of Amsterdam; and Center for High-Energy Astrophysics, Kruislaan 403, 1098 SJ Amsterdam; peterj@astro.uva.nl, michiel@astro.uva.nl, homan@nl, astro.uva.nl, mariano@astro.uva.nl, ecford@astro.uva.nl.

[2] MIT, Center for Space Research, Cambridge, MA 02139; Chandra Fellow; rudy@space.mit.edu.

[3] University of Alabama, Huntsville.

[4] Facultad de Ciencias Astronómicas y Geofísicas, Universidad Nacional de La Plata, Paseo del Bosque S/N, 1900 La Plata, Argentina.

[5] Space Research Organization Netherlands, Sorbonnelaan 2, 3584 CA Utrecht, The Netherlands; e.kuulkers@sron.nl.

[6] Astronomical Institute, Utrecht University, P.O. Box 80000, 3507 TA Utrecht, The Netherlands.

[7] Department of Physics and Astronomy, University of Illinois at Urbana-Champaign, Urbana, IL 61801; f-lamb@uiuc.edu.

atoll sources (including the millisecond X-ray pulsar SAX J1808.4−3658; Wijnands & van der Klis 1998a, Chakrabarty & Morgan 1998), and black hole candidates. The Z sources followed a slightly different correlation. In a similar analysis, Psaltis et al. (1999b) have pointed out correlations between the frequencies of some of these QPOs and other noise components in atoll sources, Z sources, and black hole candidates, which suggests these phenomena may be closely related across these various source types, or at least depend on a third phenomenon in the same manner. Because of these correlations, models describing the kilohertz QPOs that also predict QPOs or noise components in the low-frequency part of the power spectrum can be tested by investigating this low-frequency part.

In this paper, we study the full power spectral range of the bright LMXB and Z source GX 340+0 in order to investigate further the similarities between the atoll sources and the Z sources and to help constrain models concerning the formation of the different QPOs. We report on the discovery of two new components in the power spectra of GX 340+0 with frequencies less than 40 Hz when the source is on the left part of the HB. We also discuss the properties of the NBO and those of the kilohertz QPOs.

2. OBSERVATIONS AND ANALYSIS

The Z source GX 340+0 was observed 24 times in 1997 and 1998 with the proportional counter array (PCA; Jahoda et al. 1996) on board the *RXTE* satellite (Bradt, Rothschild, & Swank 1993). A log of the observations is presented in Table 1. Some of these data (observations 1 and 9–18) were used by Jonker et al. (1998) in the discovery of the kilohertz QPOs in GX 340+0. The total amount of good data obtained was ∼390 ks. During ∼19% of the time, only three or four of the five PCA detectors were active.

The data were obtained in various modes, of which the Standard 1 and Standard 2 modes were always active. The Standard 1 mode has a time resolution of 1/8 s in one energy band (2–60 keV). The Standard 2 mode has a time resolution of 16 s, and the effective 2–60 keV PCA energy range is covered by 129 energy channels. In addition, high time resolution data (with a resolution of 244 μs or better for the 2–5.0 keV band and with a resolution of 122 μs or better for the 5.0–60 keV range) were obtained for all observations.

For all observations except observation 1, which had only four broad energy bands, and observation 22, for which technical problems with the data occurred, we computed power spectra in five broad energy bands (2–5.0, 5.0–6.4, 6.4–8.6, 8.6–13.0, and 13.0–60 keV) with a Nyquist frequency of 256 Hz dividing the data into segments of 16 s length each. We also computed power spectra for all observations using 16 s data segments in one combined broad energy band ranging from 5.0 to 60 keV with a Nyquist frequency of 4096 Hz.

To characterize the properties of the low-frequency part (1/16–256 Hz) of the power spectrum we experimented with several fit functions (see § 3) but finally settled on a fit function that consisted of the sum of a constant to represent the Poisson noise, one to four Lorentzians describing the QPOs, an exponentially cut-off power law component, $P \propto \nu^{-\alpha} \exp(-\nu/\nu_{\rm cut})$ to describe the low-frequency noise (LFN), and a power-law component to represent the very low frequency noise (VLFN) when the source was on the NB.

To describe the high-frequency part (128–4096 Hz or 256–4096 Hz) of the power spectrum we used a fit function that consisted of the sum of a constant and a broad sinusoid to represent the dead-time modified Poisson noise (Zhang et al. 1995), one or two Lorentzian peaks to represent the

TABLE 1

LOG OF OBSERVATIONS

Number	Observation ID	Date (yyyy-mm-dd) and Start Time (UTC)	Total On-Source Observing Time (ks)
1	20054-04-01-00	1997-04-17, 13:26:21	19.8
2	20059-01-01-00	1997-06-06, 06:05:07	34.7
3	20059-01-01-01	1997-06-06, 21:39:06	8.1
4	20059-01-01-02	1997-06-07, 11:15:05	22.1
5	20059-01-01-03	1997-06-07, 23:48:56	21.6
6	20059-01-01-04	1997-06-08, 07:51:04	22.9
7	20059-01-01-05	1997-06-09, 00:09:03	17.5
8	20059-01-01-06	1997-06-10, 01:22:46	22.0
9	20053-05-01-00	1997-09-21, 01:04:06	17.5
10	20053-05-01-01	1997-09-23, 04:09:30	11.5
11	20053-05-01-02	1997-09-25, 01:30:29	8.4
12	20053-05-01-03	1997-09-25, 09:37:51	19.3
13	20053-05-02-00	1997-11-01, 22:38:58	9.5
14	20053-05-02-01	1997-11-02, 03:32:07	9.0
15	20053-05-02-02	1997-11-02, 19:42:00	12.7
16	20053-05-02-03	1997-11-03, 01:50:07	13.9
17	20053-05-02-04	1997-11-04, 01:59:34	11.1
18	20053-05-02-05	1997-11-04, 16:18:27	7.2
19	30040-04-01-00	1998-11-13, 23:52:00	16.7
20	30040-04-01-01	1998-11-14, 13:55:00	17.3
21	30040-04-01-02	1998-11-14, 21:03:00	28.1
22	30040-04-01-03	1998-11-15, 13:48:00	17.1
23	30040-04-01-04	1998-11-15, 20:57:00	17.0
24	30040-04-01-05	1998-11-15, 09:53:00	2.6

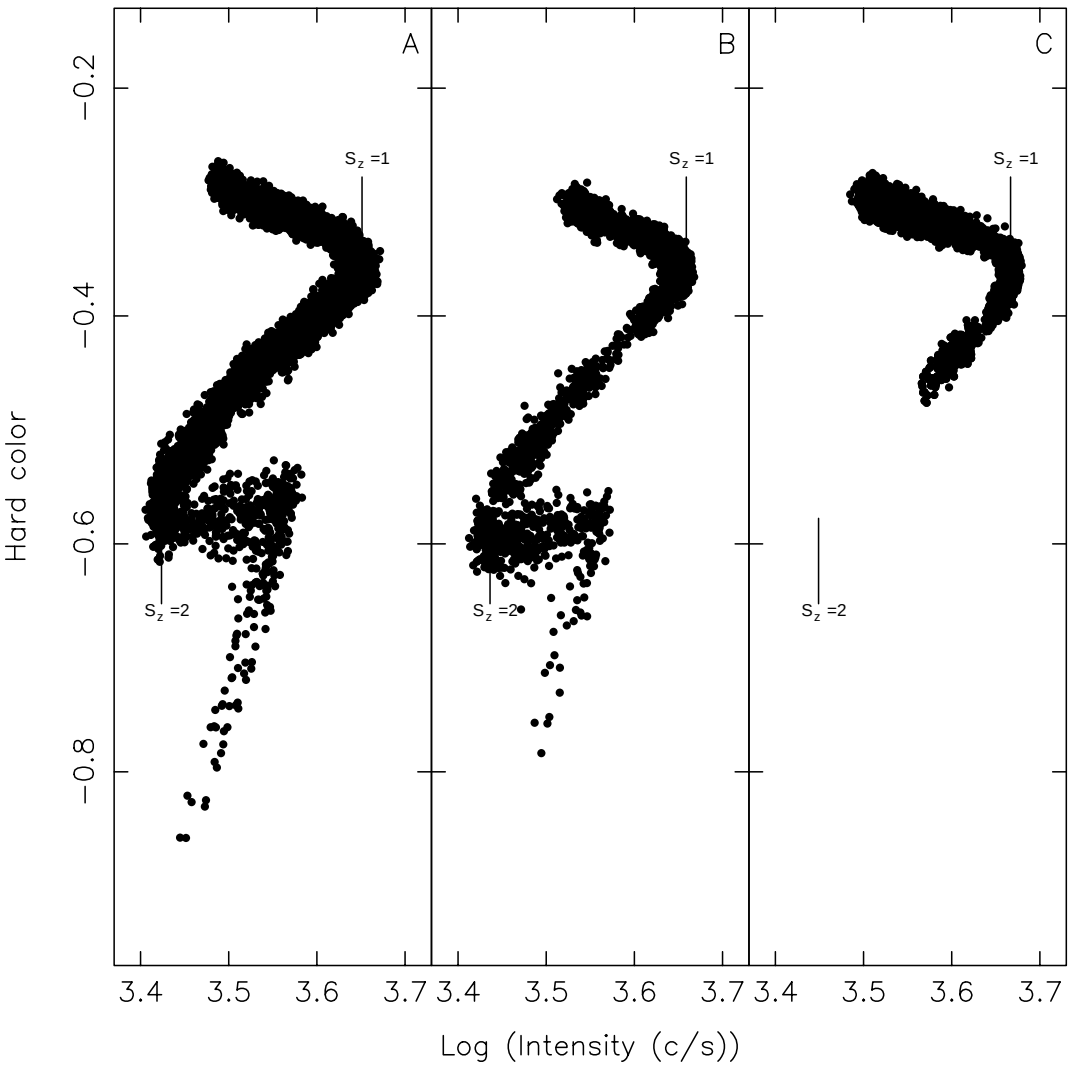

FIG. 1.—Hardness-intensity diagrams for observations 1 and 9–18 (*a*), 2–8 (*b*), and 19–24 (*c*) (see Table 1). The hard color is defined as the logarithm of the 9.7–16.0/6.4–9.7 keV count rate ratio. The intensity is defined as the three-detector count rate measured in the 2–16.0 keV band. The data were background subtracted, but no dead-time correction was applied. The dead-time correction factor was less than 1.5%.

kilohertz QPOs, and sometimes a power law to fit the lowest frequency part (<150 Hz). The PCA setting concerning the very large event window (Zhang et al. 1995; van der Klis et al. 1997) was set to 55 μs. Therefore, its effect on the Poisson noise was small, and it could be incorporated into the broad sinusoid. The errors on the fit parameters were determined using $\Delta\chi^2 = 1.0$ (1 σ single parameter). The 95% confidence upper limits were determined using $\Delta\chi^2 = 2.71$.

We used the Standard 2 data to compute hardnesses and intensities from the three detectors that were always active. Figure 1 shows three HIDs; one (*a*) for observations 1 and 9–18 combined (data set A), one (*b*) for observations 2–8 combined (data set B), and one (*c*) for observations 19–24 combined (data set C). The observations were subdivided in this way because the hard vertex, defined as the HB-NB intersection, is at higher intensities in data set C than in data set A. The hard vertex of data set B falls at an intermediate intensity level.

We assigned a value to each power spectrum according to the position of the source along the Z track using the S_Z

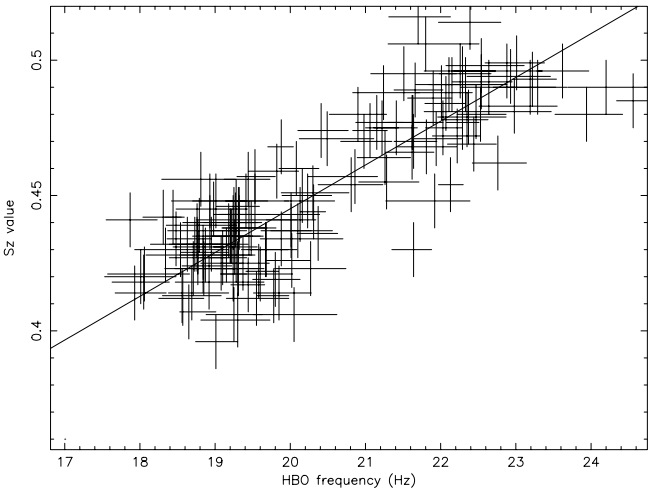

FIG. 2.—S_Z value of $\sim$150 individual 16 s length power spectra from observation 1 plotted against their fitted HBO frequency. The line represents the best linear fit. The $\chi^2_{\rm red}$ is 1.75 for 144 degrees of freedom; the linear-correlation coefficient is 0.83.

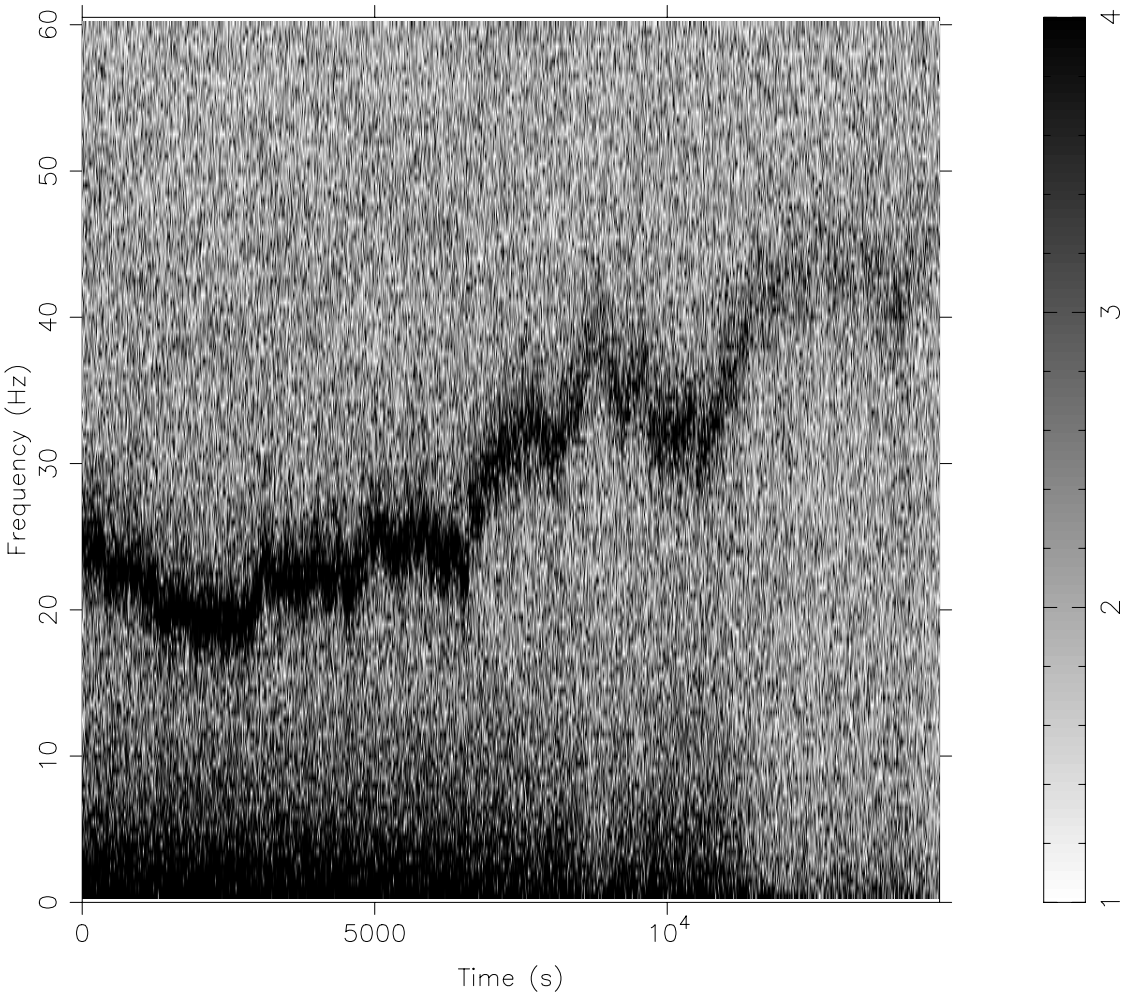

FIG. 3.—Dynamical power spectrum of part of observation 1 showing the 1/16–60 Hz range, with a frequency resolution of 0.5 Hz in the energy band 5–60 keV. The gray scale represents the Leahy normalized power (Leahy et al. 1983). Data gaps have been omitted for clarity. Clearly visible is the HBO at ~18 to ~50 Hz and the LFN component at low (<10 Hz) frequencies.

parameterization (Dieters & van der Klis 2000; Wijnands et al. 1997a) applied to each HID separately. In this parametrization, the hard vertex (defined as the HB-NB intersection) is assigned the value $S_Z = 1.0$ and the soft vertex (defined as the NB-FB intersection) is assigned $S_Z = 2.0$. Thus, the distance between the hard and soft vertex defines the length scale along each branch. Since for HID C we only observed part of the Z track, we used the position of the soft vertex of HID A in HID C. From the fact that the soft vertex of the HID B was consistent with that from HID A, we conclude that the error introduced by this is small.

The shifts in the position of the hard vertex prevented us from selecting the power spectra according to their position in an HID of all data combined. We selected the power spectra according to the S_Z value in each of the three separate Z tracks, since Jonker et al. (1998) showed that for GX 340+0 the frequency of the HBO is better correlated to the position of the source relative to the instantaneous Z track than to its position in terms of coordinates in the HID. The power spectra corresponding to each S_Z interval were averaged. However, employing this method yielded artificially broadened HBO peaks, and sometimes the HBO profile even displayed double peaks. The reason for this is that in a typical S_Z selection interval of 0.05 the dispersion in HBO frequencies well exceeds the statistical one, as shown in Figure 2. While the relation between S_Z and HBO frequency is roughly linear, the spread is large.

For this reason, when the HBO was detectable in the 5.0–60 keV power spectra, we selected those power spectra according to HBO frequency rather than on S_Z value. In practice, this was possible for all data on the HB. To determine the energy dependence of the components, the 2–5.0, 5.0–6.4, 6.4–8.6, 8.6–13.0, and 13.0–60 keV power spectra were selected according to the frequency of the HBO peak in the 2–60 keV power spectrum, when detectable.

The HBO frequency selection proceeded as follows. For each observation we constructed a dynamical power spectrum using the 5–60 keV or 2–60 keV data (see above), showing the time evolution of the power spectra (see Fig. 3). Using this method, we were able to trace the HBO frequency in each observation as a function of time. We determined the maximum power in 0.5 Hz bins over a range of 2 Hz around the manually identified QPO frequency for each power spectrum and adopted the frequency at which this maximum occurred as the HBO frequency in that power spectrum. This was done for each observation in which the HBO could be detected.

The 18–52 Hz frequency range over which the HBO was detected was divided into 16 selection bins with widths of 2 or 4 Hz, depending on the signal-to-noise ratio level. For

each selection interval the power spectra were averaged, and a mean S_Z value was determined.

The HBO selection criteria were applied to all data along the HB and near the hard vertex. When the source was near the hard vertex, on the NB, or the FB, we selected the power spectra according to the S_Z value. An overlap between the two methods occurred for data near the hard vertex; both selection methods yielded the same results for the fit parameters to well within the statistical errors (see § 3). Separately, for each set of observations (A, B, and C), we also determined the kilohertz QPO properties according to the S_Z method.

3. RESULTS

Using the fit function described by Jonker et al. (1998), which consisted of two Lorentzians to describe the HBO and the second harmonic of the HBO, and a cut-off power law to describe the LFN noise component, we obtained poor fits. Compared with Jonker et al. (1998) we combined more data, resulting in a higher signal-to- noise ratio. First we included a peaked noise component (called sub-HBO component) at frequencies below the HBO, since a similar component was found by van der Klis et al. (1997) in Sco X-1. This improved the $\chi^2_{\rm red}$ of the fit. Remaining problems were that the frequency of the second harmonic was not equal to twice the HBO frequency (similar problems fitting the power spectra on the HB of Cyg X-2 were reported by Kuulkers, Wijnands, & van der Klis 1999), and the frequency of the sub-HBO component varied erratically along the HB. Inspecting the fit showed that both the fit to the high-frequency tail of the HBO and the fit to its second harmonic did not represent the data points very well. Including an additional component in the fit function representing the high-frequency tail of the HBO (called shoulder component after Belloni et al. 1997 who used this name) resulted in a better fit to the HBO peak, a centroid frequency of the HBO second harmonic more nearly equal to twice the HBO frequency, and a more consistent behavior of the frequency of the sub-HBO component (which sometimes apparently fitted the shoulder when no shoulder component was present in the fit function).

We also experimented with several other fit function components to describe the average power spectra that were used by other authors to describe the power spectra of other LMXBs. Using a fit function built up out of a broken power law to fit the LFN component and several Lorentzians to fit the QPOs after Wijnands & van der Klis (1999b) results in significantly higher $\chi^2_{\rm red}$ values than when the fit function described in § 2 was used ($\chi^2_{\rm red} = 1.66$ for 205 degrees of freedom [dof] vs. a $\chi^2_{\rm red} = 1.28$ with 204 dof). We also fitted the power spectra using the same fit function as described in § 2 but with the frequency of the sub-HBO component fixed at 0 Hz, in order to test whether or not an extra LFN-like component centered on 0 Hz was a good representation of the extra sub-HBO component. Finally, we tested a fit function built up out of two cut-off power laws; one describing the LFN and one either describing the sub-HBO component or the shoulder component, and three Lorentzians, describing the HBO, its second harmonic, and either the sub-HBO or shoulder component when not fitted with the cut-off power law. But in all cases the $\chi^2_{\rm red}$ values obtained using these fit functions were significantly higher (for the 24–26 Hz selection range, values of 1.52 for 205 dof, 1.62 for 204 dof, and 2.00 for 205 dof were obtained, respectively).

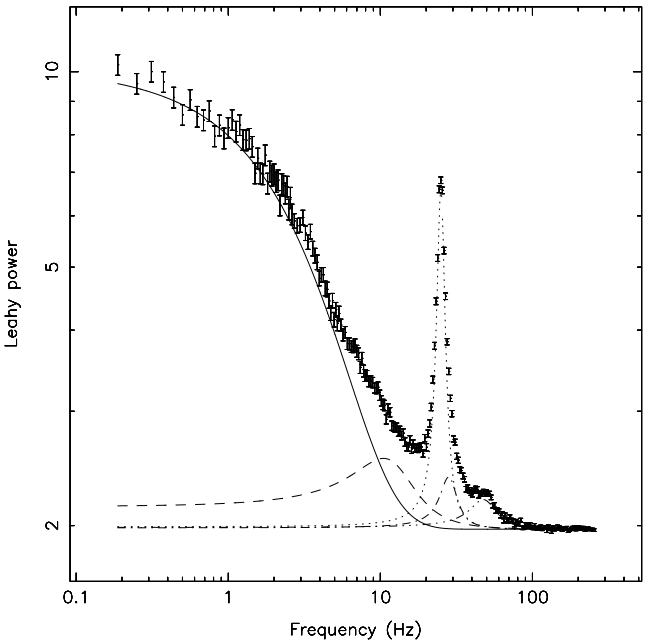

FIG. 4.—Leahy normalized power spectrum showing the different components used to fit the 5.0–60 keV power spectrum. The solid line represents the LFN component, and the constant arising in the power spectrum due to the Poisson counting noise; the dashed line represents the sub-HBO component; the dotted line represents the HBO; the dashed-dotted line represents the shoulder component; and the triple-dot–dashed line represents the harmonic of the HBO.

Settling on the fit function already described in § 2, we applied an F-test (Bevington & Robinson 1992) to the χ^2 of the fits with and without the extra Lorentzian components to test their significance. We derived a significance of more than 8 σ for the sub-HBO component, and a significance of more than 6.5 σ for the shoulder component, in the average selected power spectrum corresponding to HBO frequencies of 24–26 Hz. In Figure 4 we show the contribution of all the components used to obtain the best fit in this power spectrum.

The properties of all the components used in describing the low-frequency part of the average power spectra along the HB are given in Figure 5 as a function of S_Z. When the HBO frequency was higher than 32 Hz, the sub-HBO and shoulder component were not significant. We therefore decided to exclude these two components from the fit function in the HBO frequency selections of 32 Hz and higher. When this affected the parameters determined for the remaining components in the fit function, we mention so. Splitting the total counts into different photon energies reduced the signal-to-noise ratio in each energy band, and therefore these effects were more important in the fits performed to determine the energy dependence of the parameters.

3.1. *The LFN Component*

The fractional rms amplitude of the LFN decreased as a function of S_Z (Fig. 5*a*), with values ranging from 10% to 2.2% (5.0–60 keV). Upper limits on the LFN component were calculated by fixing the power- law index at 0.0. The power-law index of the LFN component increased from ~ 0 at $S_Z \sim 0.5$ to ~ 0.4 around $S_Z = 0.9$; when the source moved on to the NB, the index of the power law decreased

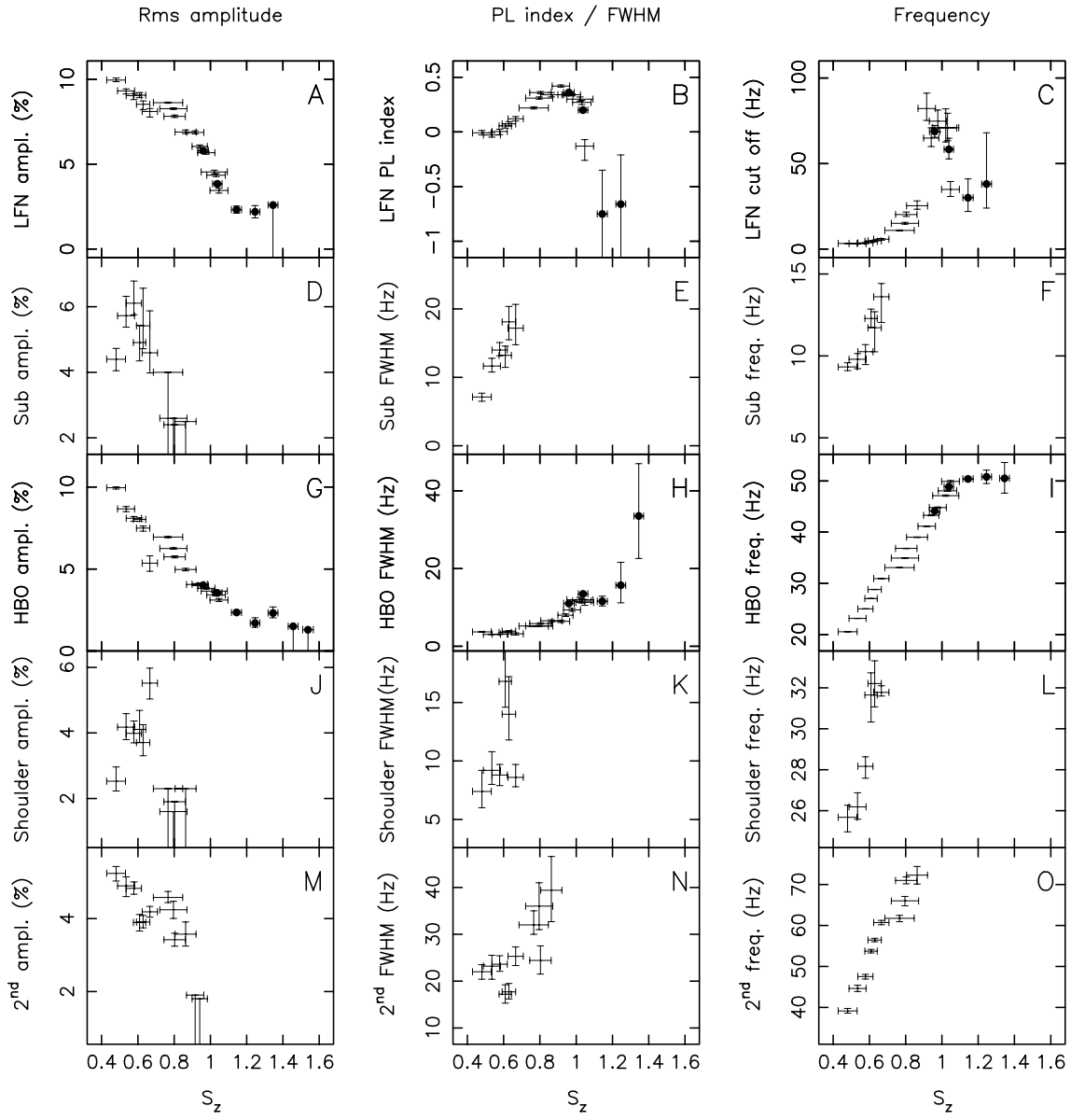

FIG. 5.—(*a*) Root mean squares amplitude of the low-frequency noise (LFN); (*b*) power-law index of the LFN; (*c*) cut-off frequency of the LFN; (*d*) rms amplitude of the noise component at frequencies below the HBO frequency (sub-HBO component); (*e*) FWHM of the sub-HBO component; (*f*) frequency of the sub-HBO component; (*g*) rms amplitude of the HBO; (*h*) FWHM of the HBO; (*i*) frequency of the HBO; (*j*) rms amplitude of the shoulder component used to describe the HBO; (*k*) FWHM of the shoulder component; (*l*) frequency of the shoulder component; (*m*) rms amplitude of the harmonic of the HBO; (*n*) FWHM of the harmonic; (*o*) frequency of the harmonic. The points represent data selected according to the HBO selection method, and the bullets represent the data selected according to the S_Z selection method (parameters measured in the 5.0–60 keV band; see text). The two methods overlap starting around $S_Z \sim 1.0$.

to values slightly below 0.0 (Fig. 5*b*). The cut-off frequency of the LFN component increased as a function of S_Z. For $S_Z > 1.0$ the cut-off frequency could not be determined with high accuracy (Fig. 5*c*).

The LFN fractional rms amplitude depended strongly on photon energy all across the selected frequency range. The rms amplitude increased from 5% at 2–5.0 keV to more than 15% at 13.0–60 keV ($S_Z = 0.48$). The power-law index, α, of the LFN component was higher at lower photon energies (changing from 0.3 to 0.5 along the HB at 2–5.0 keV) than at higher photon energies (changing from -0.2 to 0.2 along the HB at 13.0–60 keV). The cut-off frequency of the LFN component did not change as a function of photon energy.

3.2. *The HBO Component*

The fractional rms amplitude of the HBO decreased as a function of S_Z (Fig. 5*g*), with values ranging from 10% to 1.7% over the detected range (5.0–60 keV). Upper limits on the HBO component were determined using a fixed FWHM of 15 Hz. The frequency of the HBO increased as a function of S_Z, but for $S_Z > 1.0$ it was consistent with being constant around 50 Hz (Fig. 5*i*).

The ratio of the rms amplitudes of the LFN and the HBO component, of interest in beat frequency models (see Shibazaki & Lamb 1987), decreased from $\sim$1 at an S_Z value of 0.48 to $\sim$0.6 at S_Z values of 0.8–1.0. The ratio increased again to a value of $\sim$0.9 at $S_Z = 1.05$when the source was on the NB.

The HBO rms amplitude depended strongly on photon energy all across the selected frequency range. The rms amplitude increased from 5% at 2–5.0 keV to ~16% at 13.0–60 keV (at $S_Z = 0.48$) (see Fig. 6 [*filled circles*] for the HBO energy dependence in the 26–28 Hz range). The increase in fractional rms amplitude of the HBO toward higher photon energies became less as the frequency of the HBO increased. At the highest HBO frequencies the HBO is relatively stronger in the 8.4–13.0 keV band than in the 13.0–60 keV band. The ratio between the fractional rms amplitude as a function of photon energy of the HBO at lower frequencies and the fractional rms amplitude as a function of photon energy of the HBO at higher frequencies is consistent with a straight line with a positive slope. The exact fit parameters depend on the HBO frequencies at which the ratios were taken. This behavior was also present in absolute rms amplitude (≡ fractional rms amplitude $\times I_x$, where I_x is the count rate); see Figure 7. So, this behavior is caused by actual changes in the QPO spectrum, not by changes in the time-averaged spectrum by which the QPO spectrum is divided to calculate the fractional rms spectrum of the HBO. The FWHM and the frequency of the HBO were the same in each energy band.

3.3. *The Second Harmonic of the HBO*

The rms amplitude of the second harmonic of the HBO decreased as a function of S_Z (Fig. 5*m*) from 5.2% to 3.6% (5.0–60 keV). Upper limits on the second harmonic of the HBO were derived using a fixed FWHM of 25 Hz. The frequency of the second harmonic of the HBO was consistent with being twice the HBO frequency when the sub-HBO and the shoulder component were strong enough to be measured (see Figs. 5*o* and 8). When these two extra components could not be determined significantly, owing to the limited signal-to-noise ratio, and we therefore omitted them from the fit function (as explained above), the frequency of the second harmonic of the HBO was clearly less than twice the HBO frequency (see Fig. 8).

The rms amplitude of the second harmonic of the HBO was also energy dependent. Its rms amplitude increased from less than 4% in the 2–5.0 keV, to more than 9% in the

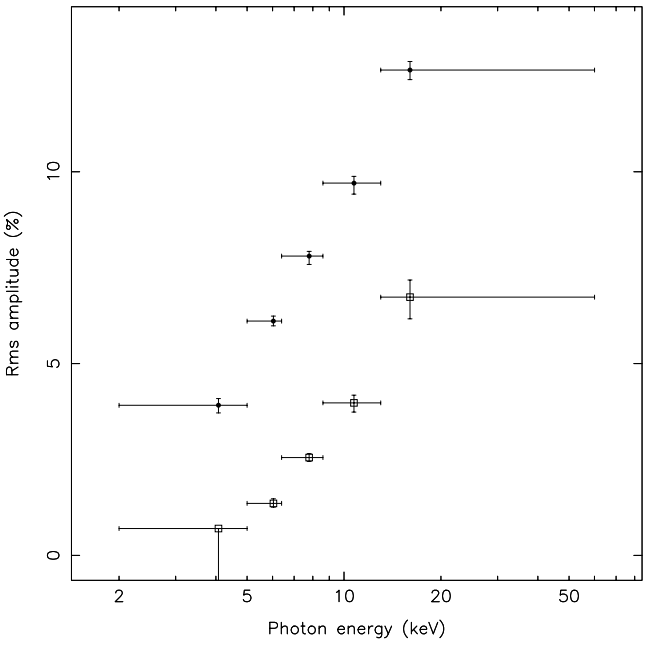

FIG. 6.—Typical energy dependence of the rms amplitude of the HBO (*filled circles*) and NBO (*squares*) as measured in the frequency range 26–28 Hz for the HBO, and as measured in the $S_Z = 1.0$–1.9 range for the NBO.

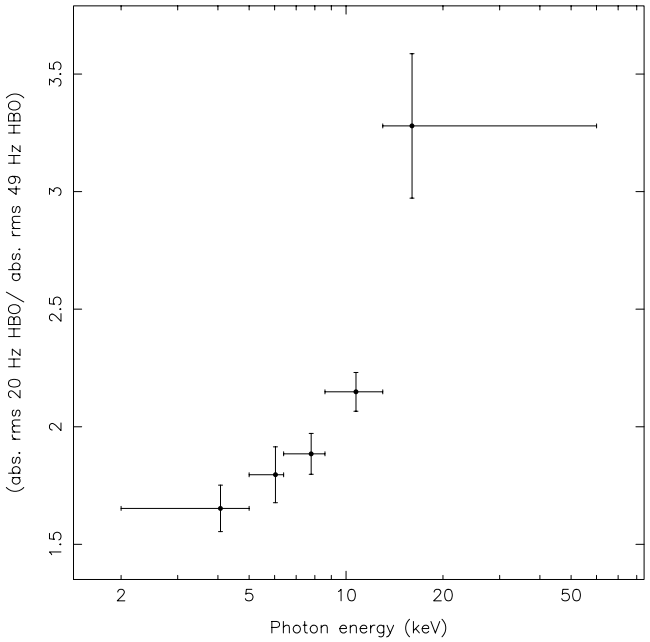

FIG. 7.—Absolute rms amplitude of the HBO at ~20 Hz divided by the absolute rms amplitude of the HBO at ~50 Hz as a function of the photon energy.

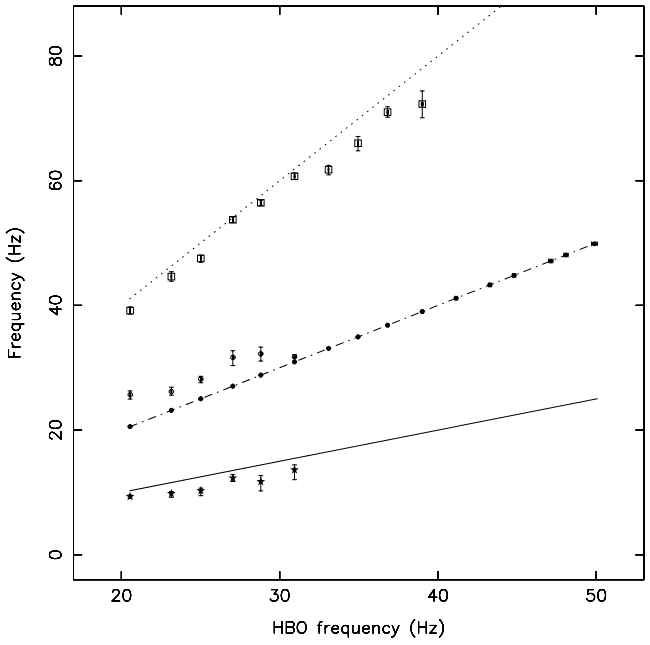

FIG. 8.—Frequencies of the four Lorentzian components used to describe the average 5.0–60 keV power spectra, as a function of the HBO frequency. Shown are from low frequencies to high frequencies; the sub-HBO component (*stars*), the HBO (*filled circles*), the shoulder component (*open circles*), and the second harmonic of the HBO (*squares*). The solid line represents the relation $\nu = 0.5\nu_{\rm HBO}$, the dash-dotted line represents $\nu = 1.0\nu_{\rm HBO}$, and the dotted line represents $\nu = 2.0\nu_{\rm HBO}$. Errors in the HBO frequency are in some cases smaller than the symbols.

8.6–13 keV band. The FWHM of the second harmonic varied erratically in the range of 10–50 Hz. This is not necessarily a property of the second harmonic since the HBO shoulder component that was not significant by itself was omitted from the fit function. This may have influenced the fit to the FWHM of the second harmonic when it was weak. Its frequency was consistent with being the same in each energy band.

3.4. *The Sub-HBO Component*

The centroid frequency (Fig. 5*f*) and FWHM (Fig. 5*e*) of the Lorentzian at sub-HBO frequencies increased from 9.3 ± 0.3 Hz to 13.6 ± 1.0 Hz and from 7.1 ± 0.6 Hz to 18 ± 3 Hz, respectively, as the source moved up the HB from $S_Z = 0.48$ to 0.67. The rms amplitude of this component did not show a clear relation with S_Z; its value was consistent with being constant around 5% (Fig. 5*d*). Upper limits on the sub-HBO component were determined using a fixed FWHM of 15 Hz. The frequency of the sub-HBO component is close to half the frequency of the HBO component. The fact that the ratio between the HBO frequency and the sub-HBO frequency is not exactly 2 but ~ 2.2 may be accounted for by the complexity of the data and therefore its description.

We detected the sub-HBO component in the three highest energy bands that we defined over an S_Z range from 0.48 to 0.65. Its rms amplitude is higher in the highest energy band ($\sim 7\%$ in 13.0–60 keV and less than 5% in 6.4–8.6 keV) and decreased as a function of S_Z, while the FWHM and the frequency increased from 6 to 12 Hz and 9 to 15 Hz, respectively.

3.5. *The HBO Shoulder Component*

At an S_Z value of 0.48 (the leftmost part of the HB) the frequency of the shoulder component was higher than the frequency of the HBO, and the frequency separation between them was largest (Figs. 5*l* and 8). Both the frequency of the shoulder and the HBO increased when the source moved along the HB, but the frequency difference decreased. The FWHM of the shoulder component increased from 7 ± 2 Hz to 17 ± 3 Hz and then decreased again to 8.6 ± 1.0 Hz as the frequency of the HBO peak increased from 25.7 ± 0.7 Hz to 30.9 ± 0.4 Hz (Fig. 5*k*). From an S_Z value of 0.61 to 0.67 the frequency was consistent with being constant at a value of 32 Hz. The rms amplitude was consistent with being constant around 4% (5.0–60 keV), over the total range at which this component could be detected (Fig. 5*j*), but the data are also consistent with an increase of fractional rms amplitude with increasing HBO frequency. Upper limits on the HBO shoulder component were determined using a fixed FWHM of 7 Hz.

In the various energy bands the HBO shoulder component was detected 7 times in total; once in the 2–5.0 keV band, 3 times in the 6.4–8.6 keV band, and 3 times in the in the 8.6–13.0 keV band, with rms amplitudes increasing from $\sim 3\%$ in the 2–5.0 keV band to $\sim 6\%$ in the 8.6–13.0 keV band, and a FWHM of ~ 10 Hz. Upper limits of the order of 3%–4% and of 5%–7% were derived in the two lowest and three highest energy bands considered, respectively. These are comparable with or higher than the rms amplitudes of this component determined in the 5–60 keV band.

3.6. *The NBO Component*

The NBOs were not observed when the source was on the HB, with an upper limit of 0.5% just before the hard vertex (for an S_Z value of 0.96). They were detected along the entire NB, and they evolved into a broad noise component on the FB. The properties are listed in Table 2. The rms amplitude of the NBO gradually increased while the source moved from the upper NB to the middle part of the NB where the rms amplitude is highest. On the lower part of the NB the NBO rms amplitude gradually decreased. Upper limits on the NBO components were determined using a fixed FWHM of 5 Hz.

As the NBO got stronger toward the middle of the NB, the profile of the NBO became detectably asymmetric (see Fig. 9); between $S_Z = 1.25$ and 1.54 the NBO was fitted using two Lorentzians. The FWHM of the NBO as a function of the position along the NB was first decreasing from ~ 10 Hz at $S_Z = 1.038$ to around 2.5 Hz on the middle part of the NB (S_Z values from 1.25 to 1.54) and then increased again to ~ 5 Hz on the lowest part of the NB.

Owing to the fact that the NBO profiles had to be fitted using two Lorentzians in part of the data, the behavior of the NBO frequency as a function of S_Z is also not determined unambiguously. Therefore, we weighted the fre-

TABLE 2

PROPERTIES OF THE NBO FITTED USING ONE OR TWO LORENTZIANS, AS A FUNCTION OF S_z IN THE 5.0–60 keV BAND

	NBO			SHOULDER			TOTAL	
S_Z	ν_{NBO} (Hz)	FWHM (Hz)	rms (%)	$\nu_{shoulder}$ (Hz)	FWHM (Hz)	rms (%)	$\nu_{weighted}$ (Hz)	Total rms (%)
0.96 ± 0.03.....	8[a]	5[a]	< 0.5	...	...	...	...	...
1.04 ± 0.03.....	6.2 ± 0.4	10 ± 2	1.8 ± 0.2	8[a]	5[a]	< 1	...	...
1.14 ± 0.03.....	5.74 ± 0.07	6.3 ± 0.3	3.4 ± 0.1	8[a]	5[a]	< 2	...	...
1.25 ± 0.03.....	4.98 ± 0.07	2.2 ± 0.2	2.8 ± 0.3	6.7 ± 0.3	5.0 ± 0.4	3.1 ± 0.3	5.27 ± 0.07	4.2 ± 0.8
1.35 ± 0.03.....	5.40 ± 0.05	2.2 ± 0.2	4.1 ± 0.3	7.5 ± 0.7	5.4 ± 0.7	2.6 ± 0.4	5.74 ± 0.05	4.9 ± 1.0
1.46 ± 0.03.....	5.65 ± 0.05	2.5 ± 0.2	4.0 ± 0.2	8.4 ± 1.1	8.5 ± 1.7	2.5 ± 0.4	5.87 ± 0.05	4.7 ± 0.9
1.54 ± 0.03.....	5.67 ± 0.12	2.9 ± 0.5	3.3 ± 0.5	$7.5^{+1.4}_{-0.8}$	9^{+5}_{-2}	2.8 ± 0.6	5.83 ± 0.18	4.3 ± 1.6
1.65 ± 0.03.....	5.9 ± 0.2	5.3 ± 0.7	3.2 ± 0.1	8[a]	5[a]	< 2.3	...	...
1.75 ± 0.03.....	6.1 ± 0.3	5.2 ± 0.9	2.4 ± 0.2	...	...	...	...	...
1.85 ± 0.04.....	7.1 ± 0.8	6.7 ± 1.6	2.1 ± 0.2	...	...	...	...	...
1.95 ± 0.04.....	6.3 ± 0.9	5 ± 3	1.7 ± 0.3	...	...	...	...	...
2.05 ± 0.03.....	5.6 ± 1.4	12 ± 4	2.6 ± 0.4	...	...	...	...	...
2.15 ± 0.03.....	4^{+3}_{-10}	22^{+15}_{-8}	$3.2^{+1.6}_{-0.5}$	...	...	...	...	...

[a] Parameter fixed at this value.

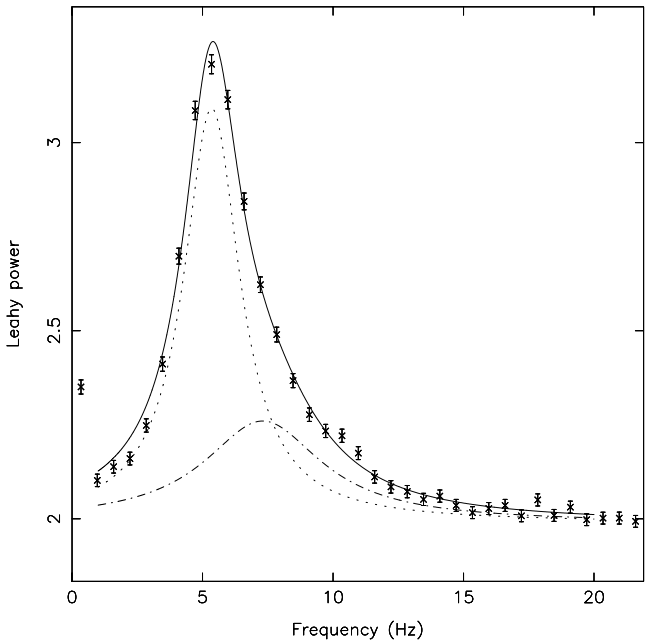

FIG. 9.—Typical Leahy normalized power spectrum on the NB showing the NBO in the energy band 5.0–60 keV (in the $S_Z = 1.2$–1.5 range). The asymmetry of the profile is clearly visible; the solid line represents the best-fit model, using two Lorentzian peaks. The dotted line and the dash-dotted line represent the two Lorentzians.

quencies of these two Lorentzians according to one over the square of the FWHM. The FWHM weighted average of the two centroid frequencies of the two Lorentzians used to describe the NBO was consistent with a small increase as a function of S_Z from 5.27 ± 0.07 Hz at $S_Z = 1.25$ to 5.83 ± 0.18 Hz at $S_Z = 1.54$.

We combined all power spectra with an S_Z between 1.0 and 1.9 in order to investigate the energy dependence of the NBO. The rms amplitude of the NBO increased as of function of photon energy (see Fig. 6 [*squares*]).

3.7. *Kilohertz QPOs*

Using the HBO frequency selection method in all data combined, the frequency of the kilohertz QPO peaks increased from 197^{+26}_{-70} Hz to 565^{+9}_{-14} Hz and from 535^{+85}_{-48} Hz to 840 ± 21 Hz for the lower and upper peaks, respectively, while the frequency of the HBO increased from 20.55 ± 0.02 Hz to 48.15 ± 0.08 Hz. Using the S_Z selection method on the three data sets we defined in § 2 (Fig. 1), we found that the relation between the kilohertz QPO and the HBO is consistent with being the same in all three data sets (Fig. 10, *upper panel*). The same relation was found when we combined all data and selected the power spectra according to the HBO frequency.

Upper limits on the kilohertz QPOs were determined with the FWHM fixed at 150 Hz. When only one of the two kilohertz QPO peaks was detected, the upper limit on the other peak was determined by fixing the frequency at the

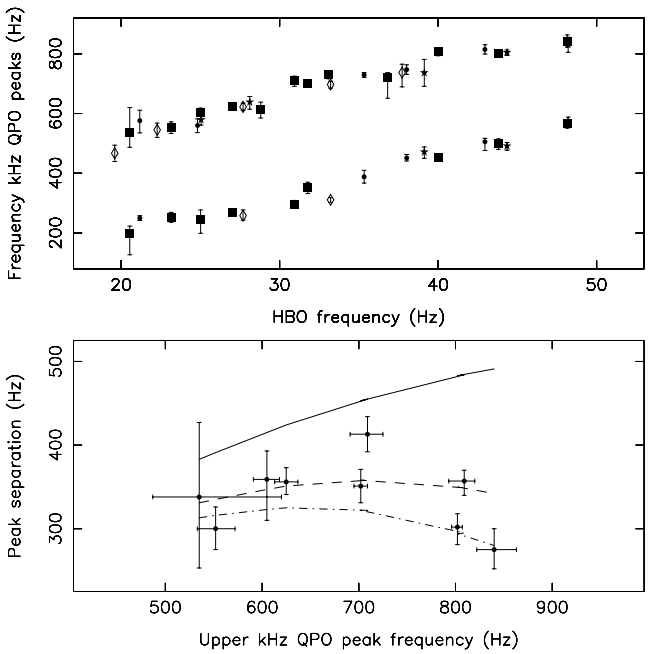

FIG. 10.—*Upper panel*: Relation between the lower and upper kilohertz QPO peak frequencies and the HBO frequency, as measured using all the data selected according to their HBO frequency in the 5–60 keV energy band (*filled large squares*), and using data from observations 1 and 9–18 combined (*filled circles*; see Jonker et al. 1998), data from observations 2–8 combined (*stars*), and data from observations 19–25 combined (*diamonds*) selected according to the S_Z selection method. The error bars on the HBO frequency are small compared to the size of the data points and are therefore omitted. *Lower panel*: The peak separation vs. upper kilohertz QPO frequency as measured when selected according to HBO frequency. The solid, dashed, and dash-dotted lines represent the predicted relations between the peak separation and the Keplerian frequency in the Stella & Vietri (1999) model for a neutron star mass of 1.4, 2.0, and 2.2 $M_\odot$, respectively.

TABLE 3

PROPERTIES OF THE KILOHERTZ QPOS AS DETERMINED IN ALL 5.0–60 keV DATA COMBINED, SELECTED ACCORDING TO THE HBO FREQUENCY

ν_{HBO} (Hz)	Upper Kilohertz ν (Hz)	FWHM Upper Peak (Hz)	rms Upper Peak (%)	Lower Kilohertz ν (Hz)	FWHM Lower Kilohertz ν (Hz)	rms Lower Peak (%)
20.55 ± 0.02.....	535^{+85}_{-48}	334^{+103}_{-172}	$4.2^{+0.8}_{-1.2}$	197^{+26}_{-70}	171^{+377}_{-94}	$3.1^{+3.7}_{-0.8}$
23.16 ± 0.02.....	552 ± 20	176 ± 43	3.3 ± 0.4	252 ± 17	125 ± 58	2.7 ± 0.5
25.02 ± 0.02.....	605 ± 14	170 ± 34	3.6 ± 0.4	246 ± 40	208^{+151}_{-85}	$2.8^{+1.0}_{-0.5}$
27.04 ± 0.02.....	625 ± 12	156 ± 36	3.3 ± 0.3	269 ± 11	63 ± 25	2.0 ± 0.3
28.81 ± 0.03.....	614 ± 27	229^{+118}_{-80}	3.1 ± 0.6	275[a]	150[a]	< 1.4
30.94 ± 0.04.....	709 ± 17	189 ± 50	3.4 ± 0.4	296 ± 12	100 ± 38	2.5 ± 0.4
31.8 ± 0.3	702 ± 7	83 ± 18	2.7 ± 0.2	351 ± 19	152^{+92}_{-52}	2.4 ± 0.5
33.09 ± 0.02.....	729 ± 13	119 ± 31	2.7 ± 0.3	390[a]	150[a]	< 2.4
36.82 ± 0.05.....	720^{+17}_{-69}	209^{+389}_{-71}	$3.5^{+2.7}_{-0.5}$	382[a]	150[a]	< 2.4
40.00 ± 0.06.....	809 ± 14	86 ± 49	$1.9^{+0.2}_{-0.4}$	452 ± 7	35 ± 27	1.2 ± 0.3
43.81 ± 0.07.....	802 ± 6	62^{+30}_{-18}	1.8 ± 0.3	500 ± 18	73 ± 31	1.3 ± 0.2
48.15 ± 0.08.....	840 ± 21	109 ± 61	1.2 ± 0.3	565 ± 12	69^{+46}_{-29}	1.1 ± 0.2

[a] Parameter fixed at this value.

frequency of the detected peak plus or minus the mean difference frequency between the two peaks, depending on whether the lower or the upper peak was detected. The properties of the kilohertz QPOs as determined in all data combined when selected according to the HBO frequency are listed in Table 3.

The kilohertz QPO peak separation was consistent with being constant at 339 ± 8 Hz over the observed kilohertz QPO range (Fig. 10, *lower panel*), but a decrease toward higher upper peak frequencies similar to that found in Sco X-1 (van der Klis et al. 1997), 4U 1608−52 (Méndez et al. 1998), 4U 1735−44 (Ford et al. 1998b), 4U 1702−429 (Markwardt, Strohmayer, & Swank 1999), and 4U 1728−34 (Méndez & van der Klis 1999) cannot be excluded. The FWHM of neither the lower nor the higher frequency kilohertz QPO peak showed a clear relation with frequency. The rms amplitude of the lower and upper kilohertz QPO peak decreased from 3.1% to 1.1% and from 4.2% to 1.2%, respectively, when the HBO frequency increased from 20.55 to 48.15 Hz.

4. DISCUSSION

In the present work we combined all *RXTE* data presently available for the Z source GX 340+0 using our new selection method based on the frequency of the HBO peak. This allowed us to distinguish two new components in the low-frequency part of the power spectrum.

These two extra components were strongest when the source was at the lowest count rates on the HB (see Fig. 1), between $S_Z = 0.48$ and 0.73, i.e., at the lowest inferred $\dot{M}$. The frequency of one of these components, the sub-HBO component, is close to half the frequency of the HBO component. The frequency ratio was consistent with being constant when the frequency of the sub-HBO changed from 9 to 14 Hz. A similar feature at sub-HBO frequencies has been reported by van der Klis et al. (1997) in Sco X-1. Since the frequency of this component is close to twice the predicted Lense-Thirring (LT) precession frequency for rapidly rotating neutron stars (Stella & Vietri 1998), we shall discuss the properties of this component within this framework.

The other component we discovered, the HBO shoulder component, was used to describe the strong excess in power in the HBO profile toward higher frequencies. If this shoulder component is related to the HBO and not to a completely different mechanism that by chance results in frequencies close to the frequency of the HBO, it can be used to constrain the formation models of the HBO peak. We demonstrated that both the HBO and the NBO have a similar asymmetric profile. In the NBO this was previously noted by Priedhorsky et al. (1986) in Sco X-1. We shall consider the hypothesis that the formation of this shoulder is a common feature of the two different QPO phenomena, even if the two peaks themselves perhaps occur owing to completely different physical reasons.

Our results on the kilohertz QPOs based on more extensive data sets at three different epochs and using the new HBO selection method are consistent with those of Jonker et al. (1998). We discuss the properties of the kilohertz QPOs within the framework of precessing Keplerian flows (Stella & Vietri 1999), the sonic point model (Miller, Lamb, & Psaltis 1998), and the transition layer model described by Osherovich & Titarchuk (1999), and Titarchuk, Osherovich, & Kuznetsov (1999).

4.1. *Comparison with Other Observations*

In various LMXBs, QPOs have been found, the profiles of which are clearly not symmetric. Belloni et al. (1997) showed that for the black hole candidate (BHC) GS 1124−68, the QPO profiles are asymmetric, with a high-frequency shoulder. Dieters et al. (1998) reported that the 2.67 Hz QPO of the BHC 4U 1630−47 was also asymmetric with a high-frequency shoulder. In the Z source Sco X-1, the NBO profile was also found to be asymmetric (Priedhorsky et al. 1986). It is clear that asymmetric shapes of the QPO profiles are frequently observed in LMXBs and are not restricted to either the black hole candidates or the neutron star systems.

In the BHCs GS 1124−68 (Belloni et al. 1997) and XTE J1550−564 (Homan et al. 1999), several QPOs were discovered that seem to be harmonically related in the same way as we report for GX 340+0, i.e., the third harmonic is not detected, while the first, the second, and the fourth harmonic are. If this implies that these QPOs are the same, models involving the magnetic field of the neutron star for their origin could be ruled out. The time lag properties of the harmonic components of the QPOs in XTE J1550−564 are complex and quite distinctive (Wijnands, Homan, & van der Klis 1999a). In GX 340+0 no time lags of the harmonic components could be measured, but the time lags measured in the HBO in the similar Z source GX 5-1 (Vaughan et al. 1994) are quite different.

In order to study in more detail the relationship found by Wijnands & van der Klis (1999a) between the QPOs and the noise break frequency in the power spectrum of LMXBs, we fitted the LFN component using a broken power law. To determine the value for the break frequency, we fixed the parameters of all other components to the values found when using a cut-off power law to describe the LFN. Wijnands & van der Klis (1999b) reported that the Z sources did not fall on the relation between the break and QPO frequency established by atoll sources and black hole candidates. They suggested that the Z source LFN is not similar to the atoll HFN but the noise component found in Sco X-1 at sub-HBO frequencies is. By using the centroid frequency of that peaked noise component as the break frequency instead of the LFN break frequency, the HBO frequencies did fall on the reported relation. On the other hand, we find that using the sub-HBO frequency instead of the HBO frequency together with the LFN break frequency, the Z source GX 340+0 also falls exactly on the relation. Therefore, the suggestion made by Wijnands & van der Klis (1999b) that the strong band-limited noise in atoll and Z sources has a different origin is only one of the two possible solutions to the observed discrepancy. Our proposed alternative solution is that the Z and atoll noise components are the same but that it is the sub-HBO in Z sources that corresponds to the QPO in atoll sources. An argument in favor of the noise components in Z and atoll sources being the same is that the cut-off frequency of the LFN component increased as a function of S_Z, in a fashion similar to that of s the frequency associated with the atoll high-frequency noise (van der Klis 1995; Ford & van der Klis 1998; van Straaten et al. 1999).

Following Psaltis et al. (1999b) we plotted the sub-HBO frequency against the frequency of the lower frequency kilohertz QPO. The sub-HBO does not fall on the relation found by Psaltis et al. (1999b) between the frequency of the

HBO and the lower frequency kilohertz QPO frequency. Instead the data points fall between the two branches defined by the HBO-like QPO frequencies versus the lower kilohertz QPO frequency at high frequencies (see Psaltis et al. 1999b).

4.2. *HBO–Kilohertz QPO Relations*

4.2.1. *Lense-Thirring Precession Frequency*

Stella & Vietri (1998) recently considered the possibility that the HBO is formed owing to the LT precession of the nodal points of slightly tilted orbits in the inner accretion disk, but as they already mentioned, the Z sources GX 5-1 and GX 17+2 did not seem to fit in this scheme. For reasonable values of I/M, the neutron star moment of inertia divided by its mass, the observed frequencies were larger by a factor of ~ 2 than the predicted ones. Jonker et al. (1998) showed that for GX 340+0, the predicted frequency is too small by a factor of 3, if one assumes that the higher frequency peak of the kilohertz QPOs reflects the Keplerian frequency of matter in orbit around the neutron star and that the mean peak separation reflects the neutron star spin frequency. Using the same assumptions Psaltis et al. (1999a) also concluded that a simple LT precession frequency model is unable to explain the formation of HBOs in Z sources.

Detailed calculations of Morsink & Stella (1999) even worsen the situation, since their calculations lower the predicted LT frequencies. They find that the LT precession frequencies are approximately a factor of 2 too low to explain the noise components at frequencies $\sim$20–35 Hz observed in atoll sources (4U 1735−44, Wijnands et al. 1998c; 4U 1728−34, Strohmayer et al. 1996, Ford & van der Klis 1998). Stella & Vietri (1998) already put forward the suggestion that a modulation can be produced at twice the LT precession frequency if the modulation is produced by the two points where the inclined orbit intersects the disk plane (although they initially used this for explaining the discrepancy of a factor of 2 between the predicted and the observed LT precession frequencies for the Z sources).

The sub-HBO peaked noise component we discovered could be harmonically related to the HBO component. If the sub-HBO is the second harmonic of the fundamental LT precession frequency, as needed to explain the frequencies in the framework of the LT precession model where the neutron star spin frequency is approximately equal to the frequency of the kilohertz QPO peak separation, the HBO must be the fourth and the harmonic of the HBO must be the eighth harmonic component, whereas the sixth and uneven harmonics must be much weaker. This poses strong (geometrical) constraints on the LT precession process. On the other hand, if the HBO frequency is twice the LT precession frequency, which implies a neutron star spin frequency of $\sim$900 Hz (see Morsink & Stella 1999), the frequency of the sub-HBO component is the LT precession frequency, and the frequency of the second harmonic of the HBO is 4 times the LT precession frequency. In that case only even harmonics and the LT precession frequency are observed.

4.2.2. *Magnetospheric Beat Frequency and Radial-Flow Models*

In this section, we discuss our findings concerning the QPOs and the LFN component in terms of the magnetic beat frequency model where the QPOs are described by harmonic series (e.g., Shibazaki & Lamb 1987).

If the sub-HBO frequency is proved not to be harmonically related to the HBO, the sub-HBO peak might be explained as an effect of fluctuations entering the magnetospheric boundary layer periodically. Such an effect will be strongest at low HBO frequencies since its power density will be proportional to the power density of the LFN (Shibazaki & Lamb 1987). If it is the fundamental frequency and the HBO its first overtone, then the magnetospheric beat frequency model proposed to explain the HBO formation (Alpar & Shaham 1985; Lamb et al. 1985) is not strongly constrained.

Within the beat frequency model the high-frequency shoulder of the HBO peak can be explained as a sign of radial drift of the blobs as they spiral in after crossing the magnetospheric boundary layer (Shibazaki & Lamb 1987). Shibazaki & Lamb (1987) describe another mechanism that may produce a high-frequency shoulder. Interference between the LFN and the QPO caused by a nonuniform phase distribution of the blobs will also cause the QPO to become asymmetric. This effect will be strongest when the LFN and the QPO components overlap, as observed. Finally, an asymmetric initial distribution of frequencies of the blobs when entering the magnetospheric boundary layer may also form an asymmetric HBO peak.

The changes in the power-law index of the LFN as a function of photon energy can be explained by varying the width or the steepness of the lifetime distribution of the blobs entering the magnetic boundary layer (Shibazaki & Lamb 1987). The decrease in increase of both the fractional and absolute rms amplitude of the HBO as a function of energy toward higher frequencies (Fig. 7) also constrains the detailed physical interactions occurring in the boundary layer.

Fortner, Lamb, & Miller (1989) proposed that the NBO is caused by oscillations in the electron scattering optical depth at the critical Eddington mass accretion rate. How a high-frequency shoulder can be produced within this model is not clear. Both the HBO and the NBO shoulder components were detected when the rms amplitude of the HBO and the NBO was highest. In case of the NBO, this may be a result of the higher signal-to-noise ratio. Since the rms amplitude of the NBO shoulder component is consistent with being $\sim 2/3$ of the NBO rms amplitude (see Table 2), combining more observations should increase the range over which this shoulder component is detected, if this ratio is constant along S_Z. In case of the HBO the two components seem to merge. While the fractional rms amplitude of the HBO shoulder component increased, that of the HBO decreased. When the fractional rms amplitudes were comparable, the HBO was fitted with one Lorentzian. The rms amplitude of both shoulder components increased in a similar way as the rms amplitudes of the NBO and the HBO with photon energy. So, the formation of these shoulder components seems a common feature of both QPO-forming mechanisms.

4.2.3. *Radial Oscillations in a Viscous Layer*

In Sco X-1, Titarchuk et al. (1999) interpreted the extra noise component in the power spectra (van der Klis et al. 1997) as due to radial oscillations in a viscous boundary layer (Titarchuk & Osherovich 1999). If the noise component in Sco X-1 is the sub-HBO component in GX 340+0, the model of Titarchuk & Osherovich (1999) can be applied to the frequencies and dependencies we found for

the sub-HBO component in GX 340+0. Fitting our data to the relation between the frequency of the extra noise component and the Keplerian frequency, using the parameters and parametrization given by Titarchuk et al. (1999), we obtained a value of $C_N = 15$ for GX 340+0. This value is much larger than the value obtained for Sco X-1 (9.76). According to Titarchuk & Osherovich (1999), a higher C_N value implies a higher viscosity for the same Reynolds number.

4.3. *Kilohertz QPOs and Their Peak Separation*

Recently, Stella & Vietri (1999) have put forward a model in which the formation of the lower kilohertz QPO is due to the relativistic periastron precession (apsidal motion) of matter in (near) Keplerian orbits. The frequency of the upper kilohertz QPO peaks is the Keplerian frequency of this material. The peak separation is then equal to the radial frequency of matter in a nearly circular Keplerian orbit and is predicted to decrease as the Keplerian frequency increases and approaches the predicted frequency at the marginally stable circular orbit. This model can explain the decrease in peak separation as observed in various sources (see § 3.7).

Beat frequency models stating that the upper kilohertz QPO peak is formed by Keplerian motion at a preferred radius in the disk (e.g., the sonic point radius; Miller et al. 1998), whereas the lower kilohertz QPO peak formed at the frequency of the beat between the neutron star spin frequency and this Keplerian frequency, cannot in their original form explain the decrease in peak separation in these two sources. A relatively small extension of the model (Lamb, Miller, & Psaltis 1999) can, however, produce the observed decrease in peak separation.

Osherovich & Titarchuk (1999) developed a model in which the kilohertz QPOs arise owing to radial oscillations of blobs of accreting material at the magnetospheric boundary. The lower kilohertz QPO frequency is in their model identified with the Keplerian frequency. Besides this QPO, two eigenmodes are identified, the frequencies of which coincide with the upper kilohertz QPO peak frequency and the frequency of the HBO component in the power spectra of Sco X-1 (Titarchuk & Osherovich 1999). Interpreting our findings within this framework did not result in stringent constraints on the model.

We found that the peak separation is consistent with being constant (Figs. 10*a* and 10*b*), but neither a decrease toward higher $\dot{M}$ as in Sco X-1, 4U 1608−52, 4U 1735−44, 4U 1702−429, and 4U 1728−34 nor a decrease toward lower $\dot{M}$, as predicted by Stella & Vietri (1999), can be ruled out. If the model of Stella & Vietri turns out to be the right one, the mass of the neutron star most likely is in the range of 1.8–2.2 $M_\odot$ (see Fig. 10*b*). This is in agreement with the mass of Cyg X-2 derived by Orosz & Kuulkers (1999) and with the masses of the neutron stars derived when interpreting the highest observed kilohertz QPO frequencies as due to motion at or near the marginally stable orbit (Kaaret, Ford, & Chen 1997; Zhang, Strohmayer, & Swank 1997).

This work was supported in part by the Netherlands Organization for Scientific Research (NWO) grant 614-51-002. This research has made use of data obtained through the High Energy Astrophysics Science Archive Research Center Online Service, provided by the NASA/Goddard Space Flight Center. This work was supported by NWO Spinoza grant 08-0 to E. P. J. van den Heuvel. M. M. is a fellow of the Consejo Nacional de Investigaciones Científicas y Técnicas de la República Argentina. Support for this work was provided by the NASA through the Chandra Postdoctoral Fellowship grant number PF9-10010 awarded by the Chandra X-ray Center, which is operated by the Smithsonian Astrophysical Observatory for NASA under contract NAS8-39073.

REFERENCES

Alpar, M. A., & Shaham, J. 1985, Nature, 316, 239
Belloni, T., van der Klis, M., Lewin, W. H. G., van Paradijs, J., Dotani, T., Mitsuda, K., & Miyamoto, S. 1997, A&A, 322, 857
Bevington, P. R., & Robinson, D. K. 1992, Data Reduction and Error Analysis for the Physical Sciences (New York: McGraw-Hill)
Boirin, L., Barret, D., Olive, J. F., Grindlay, J. E., & Bloser, P. F. 1999, in Broad Band Spectra of Cosmic X-Ray Sources (Proc. of the 32nd COSPAR Meeting) Adv. Space Res., in press (astro-ph/9902237)
Bradt, H. V., Rothschild, R. E., & Swank, J. H. 1993, A&AS, 97, 355
Chakrabarty, D., & Morgan, E. 1998, Nature, 394, 346
Dieters, S., Belloni, T., Kuulkers, E., Harmon, A., & Sood, R. 1998, IAU Circ. 6823
Dieters, S., & van der Klis, M. 2000, MNRAS, 311, 201
Di Salvo, T., Méndez, M., van der Klis, M., Ford, E. C., & Robba, N. R. 2000, ApJ, submitted
Ford, E. C., & van der Klis, M. 1998, ApJ, 506, L39
Ford, E. C., van der Klis, M., & Kaaret, P. 1998a, ApJ, 498, 41
Ford, E. C., van der Klis, M., van Paradijs, J., Méndez, M., Wijnands, R., & Kaaret, P. 1998b, ApJ, 508, L155
Fortner, B., Lamb, F. K., & Miller, G. S. 1989, Nature, 342, 775
Hasinger, G., & van der Klis, M. 1989, A&A, 225, 79
Homan, J., van der Klis, M., Wijnands, R., Vaughan, B., & Kuulkers, E. 1998, ApJ, 499, 41
Jahoda, K., Swank, J. H., Giles, A. B., Stark, M. J., Strohmayer, T., Zhang, W., & Morgan, E. H. 1996, Proc. SPIE, 2808, 59
Jonker, P. G., Wijnands, R., van der Klis, M., Psaltis, D., Kuulkers, E., & Lamb, F. K. 1998, ApJ, 499, L191
Kaaret, P., Ford, E. C., & Chen, K. 1997, ApJ, 480, L27
Kuulkers, E., & van der Klis, M. 1996, A&A, 314, 567
Kuulkers, E., Wijnands, R., & van der Klis, M. 1999, MNRAS, 308, 485
Lamb, F. K., Miller, M. C., & Psaltis, D. 1999, Proc. HEAD Meeting, 31, 10.05
Lamb, F. K., Shibazaki, N., Alpar, M. A., & Shaham, J. 1985, Nature, 317, 681
Leahy, D. A., Darbro, W., Elsner, R. F., Weisskopf, M. C., Sutherland, P. G., Kahn, S., & Grindlay, J. E. 1983, ApJ, 266, 160
Markwardt, C. B., Strohmayer, T. E., & Swank, J. H. 1999, ApJ, 512, L125
Méndez, M., et al. 1998, ApJ, 494, L65
Méndez, M., & van der Klis, M. 1999, ApJ, 517, L51
Miller, M. C., Lamb, F. K., & Psaltis, D. 1998, ApJ, 508, 791
Morsink, S. M., & Stella, L. 1999, ApJ, 513, 827
Oosterbroek, T., van der Klis, M., Kuulkers, E., van Paradijs, J., & Lewin, W. H. G. 1995, A&A, 297, 141
Orosz, J. A., & Kuulkers, E. 1999, MNRAS, 305, 1320
Osherovich, V., & Titarchuk, L. 1999, ApJ, 522, L113
Penninx, W., Lewin, W. H. G., Tan, J., Mitsuda, K., van der Klis, M., & van Paradijs, J. 1991, MNRAS, 249, 113
Priedhorsky, W., Hasinger, G., Lewin, W. H. G., Middleditch, J., Parmar, A., Stella, L., & White, N. 1986, ApJ, 306, L91
Psaltis, D., et al. 1999a, ApJ, 520, 763
Psaltis, D., Belloni, T., & van der Klis, M. 1999b, ApJ, 520, 262
Revnivtsev, M., Borozdin, K., & Emelyanov, A. 1999, A&A, 344, L25
Shibazaki, N., & Lamb, F. K. 1987, ApJ, 318, 767
Shirey, R. E., Bradt, H. V., & Levine, A.M. 1999, ApJ, 517, 472
Stella, L., & Vietri, M. 1998, ApJ, 492, L59
———. 1999, Phys. Rev. Lett., 82, 17
Strohmayer, T. E., Zhang, W., Swank, J. H., Smale, A., Titarchuk, L., & Day, C. 1996, ApJ, 469, L9
Titarchuk, L., & Osherovich, V. 1999, ApJ, 518, L95
Titarchuk, L., Osherovich, V., & Kuznetsov, S. 1999, ApJ, 525, L129
van der Klis, M. 1994a, A&A, 283, 469
———. 1994b, ApJS, 92, 511
———. 1995, in X-Ray Binaries, ed. W. H. G. Lewin, J. van Paradijs, & E. P. J. van der Heuvel (Cambridge: Cambridge Univ. Press), 252
———. 1998, in The Many Faces of Neutron Stars, ed. R. Buccheri, J. van Paradijs, & M. A. Alpar (Dordrecht: Kluwer), 337
———. 1999, in Proc. of the Third William Fairbank Meeting, in press (astro-ph/9812395)

van der Klis, M., Swank, J. H., Zhang, W., Jahoda, K., Morgan, E. H., Lewin, W. H. G., Vaughan, B., & van Paradijs, J. 1996, ApJ, 469, L1
van der Klis, M., Wijnands, R. A. D., Horne, K., & Chen, W. 1997, ApJ, 481, L97
van Paradijs, J., Hasinger, G., Lewin, W. H. G., van der Klis, M., Sztajno, M., Schulz, N., & Jansen, F. 1988, MNRAS, 231, 379
van Straaten, S., et al. 1999, ApJ, submitted
Vaughan, B., van der Klis, M., Lewin, W. H. G., Wijers, R. A. M. J., van Paradijs, J., Dotani, T., & Mitsuda, K. 1994, ApJ, 421, 738
Wijnands, R., Homan, J., & van der Klis, M. 1999a, ApJ, 526, L33
Wijnands, R., Méndez, M., van der Klis, M., Psaltis, D., Kuulkers, E., & Lamb, F. 1998a, ApJ, 504, L35
Wijnands, R. A. D., van der Klis, M., Kuulkers, E., Asai, K., & Hasinger, G. 1997a, A&A, 323, 399
Wijnands, R., et al. 1997b, ApJ, 490, L157
Wijnands, R. 1998b, ApJ, 493, L87
Wijnands, R., & van der Klis, M. 1998a, Nature, 394, 344
———. 1998b, Astron. Tel., 17, 1
———. 1999a, ApJ, 512, L39
———. 1999b, ApJ, 514, 939
Wijnands, R., van der Klis, M., Méndez, M., van Paradijs, J., Lewin , W. H. G., Lamb, F. K., Vaughan, B., & Kuulkers, E. 1998c, ApJ, 495, L39
Wijnands, R., van der Klis, & Rijkhorst, E. 1999b, ApJ, 512, L39
Zhang, W., Jahoda, K., Swank, J. H., Morgan, E. H., & Giles, A. B. 1995, ApJ, 449, 930
Zhang, W., Strohmayer, T. E., & Swank, J. H. 1997, ApJ, 482, L167
———. 1998, ApJ, 500, L167